Measurement and Numerical Evaluation of AC Losses in a ReBCO Roebel Cable at 4.5 K

J. van Nugteren, B. van Nugteren, P. Gao, L. Bottura, M. Dhallé, W. Goldacker, A. Kario, H. ten Kate, G. Kirby, E. Krooshoop, G. de Rijk, L. Rossi, C. Senatore, S. Wessel, K. Yagotintsev, and Y. Yang

***Abstract*—EuCARD-2 aims to research ReBCO superconducting magnets for future accelerator applications. The properties of ReBCO conductors are very different from low-temperature superconductors. To investigate dynamic field quality, stability, and normal zone propagation, an electrical network model for coated conductor cables was developed. To validate the model, two identical samples were prepared at CERN, after which measurements were taken at the University of Twente and Southampton University. The model predicts that for a Roebel cable, in a changing magnetic field applied in the perpendicular direction, hysteresis loss is much larger than coupling loss. In the case of a changing magnetic field applied parallel to the cable, coupling loss is dominant. In the first case, the experiment is in good agreement with the model. In the second case, the data can only be compared qualitatively because the calibration for the inductive measurement is not available.**

***Index Terms*—HTS, magnetization, measurement, modeling, ReBCO, Roebel cable, validation.**

I. Introduction

THE EuCARD2 [1] collaboration studies the feasibility of high temperature superconducting (HTS) magnets for future accelerators, such as the Future Circular Colider (FCC) [2]. The advantage of HTS over LTS is that they remain superconducting up to much higher magnetic fields making dipole magnets exceeding 20 T feasible. To verify this, at CERN an aligned block [3] prototype insert-magnet named Feather-M2 is under development [4], [5]. Inside the coil the cable is oriented such that the magnetic field is always parallel to the broad face of the tape, increasing the critical current by a factor 3–7 (depending on the tape manufacturer). At the same time CEA Saclay is constructing a more classical cosine theta insert-magnet [6], [7] allowing for comparison. Both magnets are wound with ReBCO coated conductor Roebel cable [8], [9], offering a high packing fraction, transposition and alignment (for aligned block) of the tapes. It is expected that the engineering current density of the tapes will still increase significantly. On short lengths very high current densities have already been achieved using Zr doping [10], [11]. When such conductors become available in longer lengths one can imagine an efficient, low cross sectional area, very high field magnet.

However, ReBCO coated conductors come with properties very different from classic LTS conductor. The tapes act as wide mono-filaments resulting in large screening/magnetization currents that may affect a magnet's field quality. The enhanced temperature margin at 4.5 K results in quench energies that are a few orders of magnitude higher than for LTS conductors. Therefore, magnets constructed with ReBCO are very stable. However, the normal zones propagate relatively slowly [12], making quench detection and protection more difficult. In view of the large stability it is an open question whether a 4.5 K HTS magnet is likely to quench at all. To get better understanding of the magnetization and thermal stability, a three-dimensional time dependent thermal-electric network model of coated conductor cable structures is developed. The model is capable of simulating Roebel, CoRC [13] and Stacked (twisted) type of cables.

To validate this model, experimental data on the magnetization and contact resistance of coated conductor cables are required. There have already been several reports on the magnetization loss in Roebel cables, measured at the University of Kyoto [14], Industrial Research Ltd [15]–[17], Ohio State University [18], [19] and KIT [20], [21]. However, data is at 77 K and at frequencies above 10 Hz (in most cases the angular dependence is not considered). Therefore, a collaborative effort within EuCARD2 was initiated to measure data more relevant to accelerator magnets (low temperature, low frequency). Two cable samples are assembled by Karlsruhe Institute of Technology (KIT), impregnated at CERN, and sent to Southampton University and the University of Twente for measurement. This paper presents the network model, the experimental setup, the sample preparation and a first comparison between the numerical prediction and the measurements.

II. Electrical Network Model

To find a time dependent solution for the system of equations in Eq. (1), shown at the bottom of the next page, Fig. 1 is solved. All the terms printed in bold are matrices, which when inside square brackets are assembled to a larger matrix. The first and second row of the equation represent Kirchoff's current

Manuscript received September 8, 2015; accepted January 19, 2016. Date of publication February 4, 2016; date of current version March 8, 2016. This work was supported in part by EuCARD-2 (EuCARD-2 is cofunded by the partners and the European Commission under Capacities 7th Framework Programme under Grant Agreement 312453).

J. van Nugteren, L. Bottura, H. ten Kate, G. Kirby, G. de Rijk, and L. Rossi are with CERN, 1211 Geneva, Switzerland (e-mail: jeroen.van.nugteren@cern.ch).

B. van Nugteren, P. Gao, M. Dhallé, E. Krooshoop, S. Wessel, and K. Yagotintsev are with the University of Twente, 7522 NB Enschede, The Netherlands.

W. Goldacker and A. Kario are with the Karlsruhe Institute of Technology, 76344 Eggenstein-Leopoldshafen, Germany.

C. Senatore is with the University of Geneva, 1205 Geneva, Switzerland.

Y. Yang is with the University of Southampton, Southampton SO17 1BJ, U.K.

Color versions of one or more of the figures in this paper are available online at http://ieeexplore.ieee.org.

Digital Object Identifier 10.1109/TASC.2016.2525919

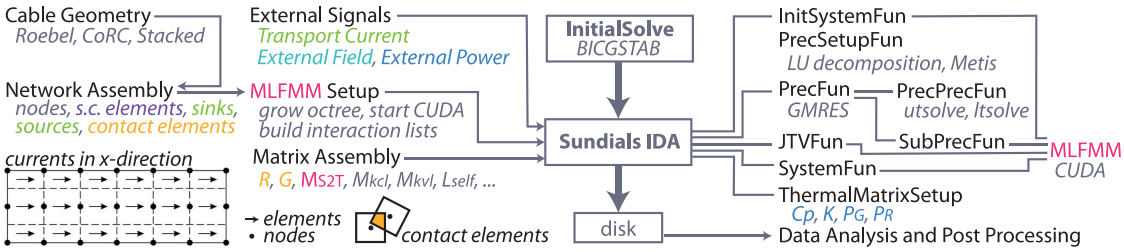

Fig. 1. Flowchart diagram showing the solver setup used to solve the electrothermal network equation presented above. The first line of the equation represents Kirchoff's current law, the second line represents Kirchoff's voltage law, and the third line represents the discrete heat equation. The colors in (1) correspond to equally colored items in the flowchart. (color citation is only available in the online version)

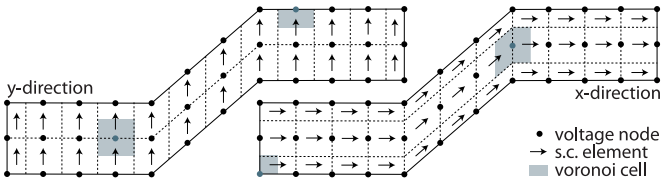

Fig. 2. Electrical network geometry with voltage nodes and superconducting elements, shown separately for the longitudinal and transverse directions. For clarity, a very coarse version of the network is shown. For a couple of nodes, the Voronoi cells used for the determination of the tape-to-tape contact areas are shown.

and voltage law, respectively [22]. The third row represents the heat equation, which is optional and can be enabled or disabled when needed.

A. Network Geometry

In the model, the tape surfaces are represented by a grid of nodes and superconducting elements also referred to as a partial element equivalent circuit [23] (PEEC) (see Fig. 2). In the matrix equation the voltages V and temperatures T are defined at the nodes, the currents I in the elements. Although the current can only flow in the longitudinal and transverse directions, when the grid is fine enough it is able to approximate the behavior of a superconducting surface. The geometry of the cable is fully defined by one unit cell, which is the shortest repeating length inside the cable (see in Fig. 3). A longer cable's network is initially constructed for a single unit cell, after which the pattern is repeated. In the unit cell the nodes of all tapes coincide at the same cross section, some of which are defined by the corners at the cross-overs. The current carrying capacity of the elements on the cross-over is artificially increased to compensate for the lower width, due to the elements being under an angle.

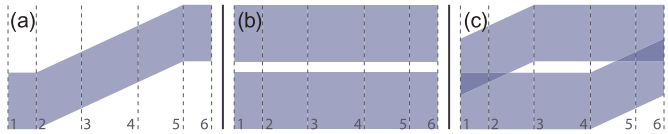

Fig. 3. Tape sections making up the geometry of the Roebel cable: (a) the cross-over bridge when located at the center of the unit cell, (b) the sloped tapes, and (c) the cross-over bridge at the edge of the unit cell.

B. Kirchoff's Voltage and Current Matrices

To couple the current to the voltage equations the voltage law matrix $\boldsymbol{M}_{kvl}$ and the current law matrix $\boldsymbol{M}_{kcl}$ are used [24]. The first calculates the voltage drop over an element by taking the differential voltage of the nodes it is connected to $V_{\text{element}} = \boldsymbol{M}_{kvl} V$. The second matrix, given as $\boldsymbol{M}_{kcl} = \boldsymbol{M}_{kvl}^T$, calculates the current flowing towards each node (which should be zero every time step), from the currents in all elements $I_{\text{node}} = \boldsymbol{M}_{kcl} I$. Additional voltage or current, for example to model an external transport current, can be supplied using V_s and I_s, respectively.

C. Superconducting Elements

The superconducting elements have a non-linear voltage-to-current behavior. This introduces hysteresis into the model, but also allows for accurate quench propagation predictions. During quench the current density of the elements strongly exceeds the critical one, therefore it is not sufficient to model these elements using a basic power law with exponent N. Instead a current sharing model is used to calculate the fraction of the total current I_0 that runs in the superconductor I_{sc}. The equation is given as

$$I_0 - \frac{E_0}{\rho(B,T)} \left[\frac{I_{\text{sc}}}{I_c(T,B,\alpha)} \right]^N - I_{\text{sc}} = 0 \qquad (2)$$

$$\begin{bmatrix} \boldsymbol{G} & \boldsymbol{M}_{kcl} & 0 \\ \boldsymbol{M}_{kvl} & -\boldsymbol{R} & 0 \\ \boldsymbol{P}_G & \boldsymbol{P}_R & \boldsymbol{K} \end{bmatrix} \begin{bmatrix} V \\ I \\ T \end{bmatrix} + \begin{bmatrix} 0 & 0 & 0 \\ 0 & \boldsymbol{L}_{\text{self}} + \boldsymbol{M}_{S2T} & 0 \\ 0 & 0 & -\boldsymbol{C}_p \end{bmatrix} \begin{bmatrix} \frac{\partial V}{\partial t} \\ \frac{\partial I}{\partial t} \\ \frac{\partial T}{\partial t} \end{bmatrix}$$
$$+ \begin{bmatrix} 0 \\ V_{nl}(I,T,B,\alpha) + V_{fmm}\left(\frac{\partial I}{\partial t}\right) + V_{bg}\left(\frac{\partial \vec{B}}{\partial t}\right) \\ P_{nl}(I_{nc}) \end{bmatrix} + \begin{bmatrix} I_s \\ V_s \\ P_s \end{bmatrix} = r = 0 \qquad (1)$$

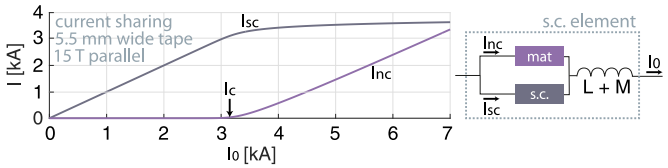

Fig. 4. Current sharing between the superconductor and the matrix as a function of the total current as calculated, using (2), for a 5.5-mm-wide tape.

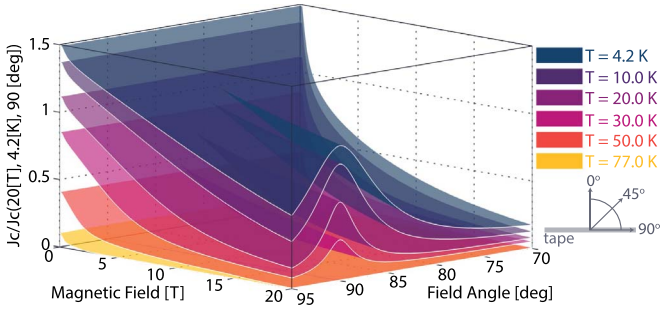

Fig. 5. Normalized critical current as a function of magnetic field, temperature, and field angle of the state-of-the-art ReBCO coated conductor.

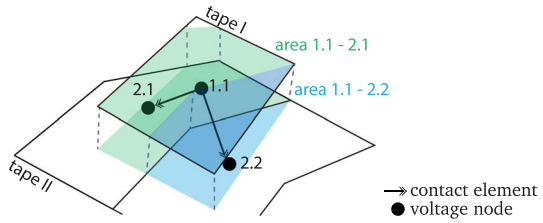

Fig. 6. Example showing the calculation of contact areas between the nodes of two tapes by projecting their respective Voronoi cells.

where ρ is the resistance of the matrix, E_0 the electric field criterion and I_c the critical current. The normal conducting current is calculated as $I_{nc} = I_0 - I_{\text{sc}}$, from which the voltage drop of the element is calculated as $V_{nl} = I_{nc}\rho$. The equation is implicit and is therefore solved numerically using a simplified version of Newton-Raphson [25] type of algorithm. As an example the current sharing between the matrix and the superconductor is presented in Fig. 4. The critical current I_c is calculated as function of temperature, magnetic field and field angle. The last two of which are calculated from the element currents using the Multi Level Fast Multipole Method (MLFMM) [26]. The normalized critical current as given by the used scaling relation [27], [28] is presented in Fig. 5. The surface was scaled to 450 A/mm (tape width), at 20 T parallel field and 4.2 K.

D. Contact Elements

During the network assembly the contact resistances between nodes of different tapes are calculated by taking the overlap between their respective Voronoi cells (see Fig. 2). The overlap is calculated in Cartesian coordinates for Roebel and Stacked cable types (as illustrated in Fig. 6), or in cylindrical coordinates for CoRC cables. From the overlapping area the resistance

Fig. 7. One of the samples after impregnation with CTD 101G still inside its impregnation mold.

is calculated from a set contact resistance, which has an estimated lower limit of 10^{-8} Ωm^2 [29], [30]. The resistances are either given on the diagonal of the resistance matrix $\boldsymbol{R}$, or as conductances in matrix $\boldsymbol{G}$ such that $I_{\text{node}} = \boldsymbol{G}V$.

E. Self and Mutual Inductance

Each element is coupled inductively with each other element and with itself. The self inductance on the diagonal of $\boldsymbol{L}_{\text{self}}$ is calculated for the superconducting elements using an equation for flat ribbons [31], [32] given as

$$L_{\text{sc}} = 0.002 \left[\log\left(\frac{2\ell}{w+t}\right) + 0.5 + 0.2235\left(\frac{w+t}{\ell}\right)\right] \quad (3)$$

where w is the width, t is the thickness and ℓ the length of the element (all in cm). For the contact elements the self inductance is calculated using an equation for round wires [33]. The MLFMM is again used, because the matrix containing all the mutual inductances is dense, which causes memory and computation time issues. With the exception of the interactions calculated during the source-to-target step are, which are represented by the $\boldsymbol{M}_{S2T}$ matrix. This matrix is needed for the approximation of the system matrix for the pre-conditioner. The other induced voltages from the MLFMM are represented by V_{fmm}.

F. Heat Equation

For the calculations presented in this paper a constant temperature of 4.5 K is assumed. For future (quench) simulations the thermal behavior of cable can also be simulated. This is achieved by coupling the electrical equations to the heat equation. The matrices $\boldsymbol{P}_G$ and $\boldsymbol{P}_R$ calculate the power generated by the contact elements, using the node-to-node voltage drop or the element currents, respectively. The conductive heat transfer is represented by matrix $\boldsymbol{K}$. The heat capacity is on the diagonal of matrix $\boldsymbol{C}_p$. These matrices are re-assembled every time step because they rely on the temperature dependent material properties. The power of the superconducting elements P_{nl} is calculated separately using I_{nc}. External power can be supplied to one or multiple nodes, for example to initiate a quench, using P_s.

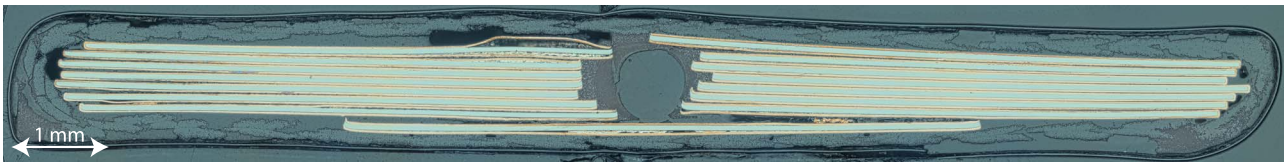

Fig. 8. Microscope recording showing the cross section of one of the impregnated Roebel samples. It should be noted that the image was taken of a cross section located at the very end of the sample. The dark line around the sample is a piece of Kapton tape.

G. Solving the System of Equations

The resulting network equations are solved using a similar solver setup as used in the Cable In Conduit Cable (CICC) model JackPot-AC [34], [35]. A flow diagram showing the different elements of the code is presented in Fig. 1. At the heart lies the sundials IDA solver [36], [37], which is written to solve equations of the form $f(t, y, y') = 0$. IDA is preconditioned using the generalized minimal residual method (GMRES), which is in turn preconditioned using LU-factorization. This train of solvers is a necessity because $V_{fmm}(\partial I/\partial t)$ is not represented by a matrix and can therefore not be solved directly. The non-linear part is of the solution is implemented using a Jacobian Times Vector (JTV) function (which is a feature of Sundials IDA).

H. Magnetization and AC-Loss Calculation

The magnetization is derived from the current using $\vec{M} = 0.5\vec{X} \times d\vec{X}I$, where X is the position vector and dX the direction vector of the elements. The magnetization loss can now be determined using two different methods: from the surface of the magnetization loop and from the resistive power dissipation of all the elements in the network. In the second case hysteresis losses can be distinguished from coupling losses by calculating the power separately for the superconducting elements and for the normal conducting elements, respectively. As an initial validation both loss factors, integrated over one cycle, are added together after which they are compared to the area of the magnetization loop (also see Section V-B). Good agreement is found between the two methods.

III. Sample Geometry and Preparation

The Roebel cable used for the two samples is punched and assembled with SuperPower tapes by KIT. The geometry of the cable follows the parameters of the Feather-M2 baseline cable [3]. The samples are fitted with a 16 mm wide S2-glass (33 Tex) sleeve, the same insulation system foreseen for the EUCARD2 magnets.

A. Impregnation Method

Both cable samples are impregnated using CTD 101G [38], which is an alumina-loaded resin. The 300 mm long mold is designed specifically to allow the filled resin to flow into the cable from the edge (see Fig. 7). This reduces the filtering of the alumina particles by the glass sleeve. An adjustment shim is added into the mold to fine-tune the pressure on the wide face of the cable to around 5 MPa. This ensures that all the tapes are in good electrical contact. The pressure was verified using Fuji paper [39]. After impregnation the cable was removed from the mold with compressed air to avoid unnecessary strain on the sample. After the impregnation the cable samples are cut at both ends to a length of 226 mm (a single transposition length) and cleaned, to ensure no electrical contact between the tapes is present at their ends.

Fig. 9. Sample holder used for ac loss measurements. Visible are the correction and pickup coils on the left and right, respectively.

B. Inspection and Microscopy

The cut ends of the samples were polished for inspection under an optical microscope (see Fig. 8). A relatively large void was observed in the resin at the central channel of the cable. Some tapes in the cable are misplaced by up to 200 μm and seem to be at least partially in contact. Some de-lamination of the copper stabilizer is observed, mainly on- or near the cross-overs. It is clear that reality is less perfect than the numerical model.

IV. Experimental Setup

The cable sample is mounted on a dedicate sample-holder (see Fig. 9) which is inserted into a time varying magnetic field of a given amplitude, angle and frequency. The resulting AC-losses are measured in two ways: calorimetric and inductively. The first is more direct and accurate, but has a high noise floor and therefore only works in high-loss scenarios. The second has a lower noise floor, but is less direct and does not always translate easily to losses.

A. Calorimetric Measurement

The losses induced by the applied field are obtained by measuring the average amount of helium that is evaporated by the sample over a relatively high number of periods. This is achieved by placing the sample inside a partially enclosed volume into which liquid helium is able to enter through the bottom and produced helium gas is able to escape at the top, where it is fed through a gas-flow-meter.

B. Inductive Measurement

The applied changing field magnetizes the sample. The changing (in time) average (in space) magnetization is measured

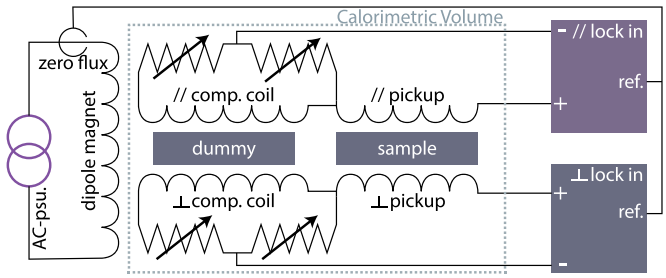

Fig. 10. Simplified electrical diagram of the experimental setup showing both the parallel and perpendicular pickup coils.

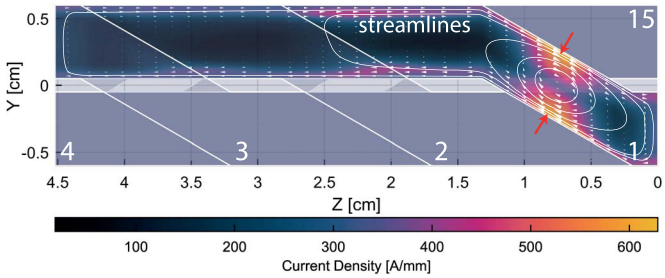

Fig. 11. Calculated current density distribution inside a tape at 2.5 s, for a 0.1-Hz applied magnetic field in the perpendicular direction, with amplitude 0.5 T and 4.5 K. Additional streamlines representing the current paths are added by hand. The tapes are numbered. High-ac-loss regions in the first tape are denoted with red arrows. Note that the units are given as current per width.

using two pickup coils: one for the perpendicular component of the magnetization and one for the parallel component. The pickup voltage consists of many frequencies and phases, but only the part of the signal, which has the same frequency as the applied field (f) and is in-phase with it contributes to the AC-losses inside the sample. This signal is measured using a lock-in amplifier as illustrated in the electrical diagram in Fig. 10. The loss per unit of volume per cycle Q is obtained using

$$Q = \mu_0 \int \vec{M} \cdot d\vec{H} = \frac{1}{2f}\left[\left(\frac{V_i H_0}{F A_e}\right)_{\perp} + \left(\frac{V_i H_0}{F A_e}\right)_{\parallel}\right] \quad (4)$$

where the $F_\perp$ and $F_\parallel$ are the "fill factors" of the sample inside the pickup coils, $V_{i,\perp}$ and $V_{i,\parallel}$ are the in-phase parts of the pickup voltages, $H_{0,\perp}$ and $H_{0,\parallel}$ are the two components of the applied field and $A_{e,\perp}$ and $A_{e,\parallel}$ are the effective areas of the two pickup coils. The quality of the measurement is improved by using a high amplification factor on the lock-in amplifier. This is only possible if the out-of-phase component of the pickup voltage is heavily suppressed, which is achieved by using a compensation coil; a coil, which only picks up the applied field and will therefore generate a purely out-of-phase voltage. A voltage divider is used to regulate the contribution of the larger compensation coil.

C. Fill Factor and Varying Current Paths

Usually the inductive measurement data is gauged to the calorimetric data, combining the higher sensitivity of the inductive method, with the accuracy of the calorimetric method. This results in a fill factor for each pickup coil. However, for the HTS Roebel cable the position of the magnetization (penetration depth) and coupling current paths can strongly depend on the selected parameters. Therefore, the data analysis and comparison need to be performed with special care.

V. Results and Validation

In this section the numerical end measured AC-loss data is presented and compared. Since losses are commonly represented per volume unit, the cable volume used is set the same for both numerical and measured data at $0.8 \times 12 \times 226$ mm^3.

A. Convergence With the Number of Elements

The convergence with number of elements over the width of the tapes is studied. Not surprisingly mainly the hysteresis loss depends on this number, which is the major loss factor in perpendicular field. At 0.5 T the solution at 14 elements is only 3% different from the 24 element solution. However, when the amplitude is low the penetration depth decreases. For 0.15 T already 36 elements are needed to obtain an accurate hysteresis loss value. For now this field is accepted as a lower limit (for hysteresis) until a better solution is found. The measurement is limited at higher fields by the voltage of the magnet power supply. This results in the data having only partial overlap.

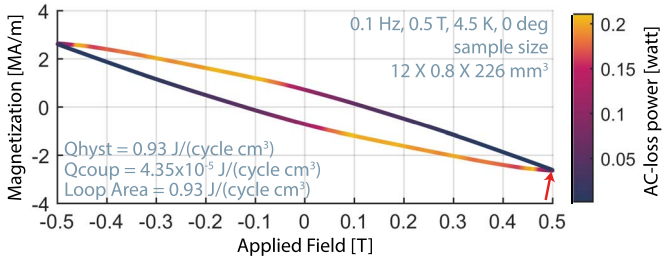

Fig. 12. Calculated magnetization loop for a 0.1-Hz applied magnetic field in the perpendicular direction, with amplitude 0.5 T and 4.5 K. The color represents the total loss, which is, in this case, dominated by hysteresis. Time of Fig. 11 is denoted with the red arrow.

B. AC-Loss Time and Position

The calculated magnetization currents inside a Roebel cable with a total length of 3 units are shown in Fig. 11. The flux penetrates much further into the tapes on the cross-overs because at this position the screening currents are not divided over seven or eight tapes, but are only flowing through the cross-over tape. A large part of the AC-loss is therefore located here, as previously found by Grilli and Zermeno [40], [41]. Although the losses are usually given per cycle (since it can be calculated as its surface area), they are not constant throughout it. The loss around the magnetization loop, calculated directly from the elements, is presented in Fig. 12.

C. Angular Dependence

The angular dependence of the AC-loss is modeled at various magnetic fields (see Fig. 13. The field angle α is defined as the angle with the face-normal. In perpendicular field the model predicts that the loss is dominated by the hysteresis and in

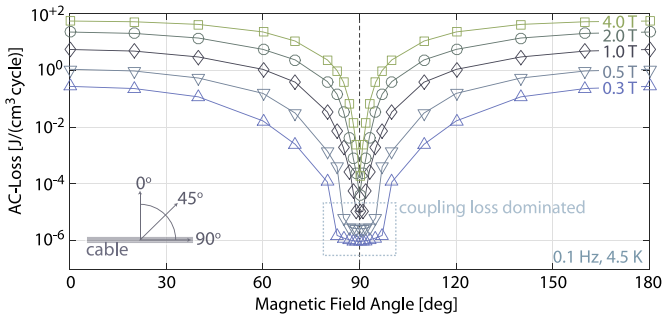

Fig. 13. Model prediction of the total ac loss as a function of field angle at 0.1 Hz and 4.5 K.

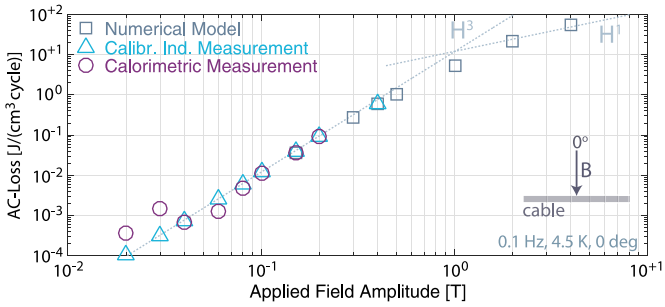

Fig. 14. AC loss as a function of magnetic field amplitude in the perpendicular direction, at a frequency of 0.1 Hz and a temperature of 4.5 K.

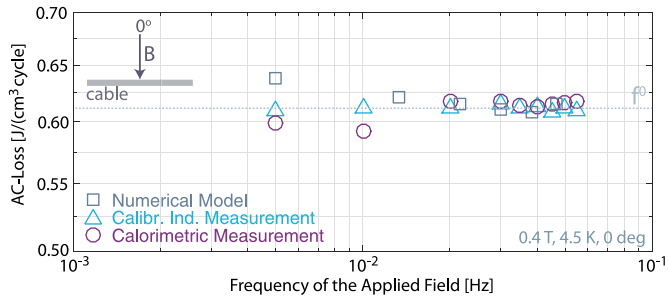

Fig. 15. AC loss as a function of frequency for a magnetic field in the perpendicular direction, at a magnetic field amplitude of 0.4 T and a temperature of 4.5 K.

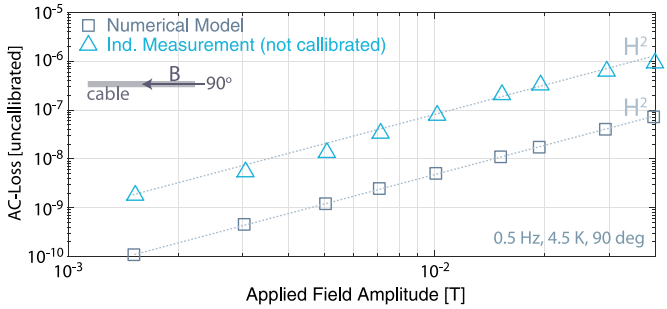

Fig. 16. AC loss as a function of magnetic field amplitude in the parallel direction, at a frequency of 0.5 Hz and a temperature of 4.5 K. Note that measurements are taken at higher frequency and lower amplitude compared with the measurements in perpendicular field. This tradeoff (the power supply is still at its maximum voltage) allows for faster and more reliable measurements.

parallel (at lower fields) by coupling. In the second case it must be noted that the model uses infinitely thin current sheets and therefore the superconductor cannot magnetize in the transverse direction.

D. Hysteresis Loss in Perpendicular Applied Field

To determine the nature of the loss in the perpendicular direction, it is measured as function of magnetic field amplitude. The results are presented in Fig. 14 in which measured data and numerical data are shown together. The inductive data are calibrated with the calorimetric data. The data scales to the third power of the magnetic field H^3, which is typical for hysteresis loss. Also, it indicates that the fill factor does not change significantly over the measured range. The numerical result overlaps with the measurement. Above field amplitudes of 1 T the data diverts from the power law towards a linear relation. This is because at this point the penetration field is reached. In addition the dependence on frequency is measured (see Fig. 15). Calibration using calorimetric measurement is again possible. No dependence is observed in both the measurement and the model. This indicates as well that hysteresis loss is the dominant term.

E. Coupling Loss in Parallel Applied Field

The amplitude dependence is also measured in the parallel direction (see Fig. 16). Because the losses are relatively small, no calorimetric data is available, leaving the measurement uncalibrated. However, it can be seen that the data scales with the second power of the magnetic field H^2. Assuming this is not distorted by a changing fill factor, this indicates pure coupling losses, which is the same as the model prediction. The model predicts a linear dependence with f, again indicative of coupling, however the measurement only sees a small frequency dependence, which could indicate a mixture of both coupling and hysteresis. The cause of this discrepancy between both sweeps is guessed to be a small misalignment of the sample during the second measurement. This can however not be verified at this time.

VI. Conclusion

A novel electrical network model capable of analyzing electrical and thermal phenomena in coated conductor cables was introduced. This model is necessary to solve critical issues in coated conductor (accelerator) magnets, such as thermal stability, quench propagation and field quality. In order to validate the model a collaborative effort within EuCARD2 was initiated to measure magnetization losses in the baseline Roebel cable. AC-losses are modeled and measured in time-varying magnetic field. When the magnetic field is perpendicular with respect to the tape surface, mainly hysteresis loss is observed. These losses are positioned for a large part on the cross-overs and vary strongly with time. In the parallel direction, coupling losses seem to become more apparent, although this is more difficult to determine with certainty because calibration with a calorimetric measurement was not feasible because the losses were too low. For the hysteresis good agreement is found with the model. Although at very low fields more elements are needed because most of the flux penetration happens on the tape edges. For

the coupling loss only qualitative agreement is found for the scaling amplitude. For the frequency scaling in parallel some discrepancy is found, possibly caused due to an alignment issue. Unfortunately a definitive value for the contact resistance is not yet determined.

REFERENCES

[1] L. Rossi *et al.*, "The EuCARD-2 future magnets project: The European collaboration for accelerator quality HTS magnets," presented at the 23rd Int. Conf. Magnet Technol., Boston, MA, USA, vol. 25, no. 3, pp. 1–7, Jun. 2015.

[2] Future Circular Colider Study. [Online]. Available: https://espace2013.cern.ch/fcc/Pages/default.aspx

[3] J. van Nugteren, G. Kirby, and G. de Rijk, "Study of a 5T HTS research dipole insert-magnet using an anisotropic ReBCO Roebel cable," *IEEE Trans. Appl. Supercond.*, vol. 25, no. 3, Jun. 2015, Art. ID 4000705.

[4] G. Kirby *et al.*, "Accelerator quality HTS dipole magnet demonstrator designs for the EuCARD2, 5 T 40 mm clear aperture magnet," in *Proc. Appl. Supercond. Conf.*, Charlotte, NC, USA, vol. 25, no. 3, pp. 1–5, Jun. 2015.

[5] G. Kirby *et al.*, "Status of the demonstrator magnets for the EuCARD2 future magnets project," in *IEEE Trans. Appl. Supercond.*, to be published.

[6] C. Lorin *et al.*, "Cos-theta design of dipole inserts made of YBCO-Roebel or BiSCCo-Rutherford cables," in *IEEE Trans. Appl. Supercond.*, vol. 25, no. 3, Jun. 2015, Art. ID 4000305.

[7] C. Loren, M. Durante, and P. Fazilleau, "Development of a Roebel-cable-based cos-theta dipole: Design and windability of magnet ends," in *Proc. EUCAS*, Lyon, France, 2015.

[8] W. Goldacker *et al.*, "ROEBEL Assembled Coated Conductors (RACC): Preparation, properties and progress," *IEEE Trans. Appl. Supercond.*, vol. 17, no. 2, pp. 3398–3401, Jun. 2007.

[9] W. Goldacker *et al.*, "REVIEW—Roebel cables from REBCO coated conductors: A one-century-old concept for the superconductivity of the future," *Supercond. Sci. Technol.*, vol. 27, no. 9, Aug. 2014, Art. ID 093001.

[10] A. Xu *et al.*, "Strongly enhanced vortex pinning from 4 to 77 K in magnetic fields up to 31 T in 15 mol. (Gd, Y)-Ba-Cu-O superconducting tapes," *Appl. Mater.*, vol. 2, no. 4, Apr. 2014, Art. ID 046111.

[11] V. Selvamanickam *et al.*, "Requirements to achieve high in-field critical current density at 30 K in heavily-doped $(Gd, Y)Ba_2Cu_3O_x$ superconductor tapes," *Supercond. Sci. Technol.*, vol. 28, no. 10, Oct. 2015, Art. ID 104003.

[12] J. van Nugteren *et al.*, "Measurement and analysis of normal zone propagation in a YBCO coated conductor at temperatures below 50 K," *Phys. Procedia*, vol. 67, pp. 945–951, 2015.

[13] C. Barth *et al.*, "Temperature- and field-dependent characterization of a conductor on round core cable," *Supercond. Sci. Technol.*, vol. 28, no. 6, Apr. 2015, Art. ID 065007.

[14] T. Komeda *et al.*, "Experimental comparison of AC loss in ReBCO Roebel cables consisting of six strands and ten strands," *IEEE Trans. Appl. Supercond.*, vol. 24, no. 3, Jun. 2014, Art. ID 8200505.

[15] L. Lakshmi, K. P. Thakur, M. P. Staines, R. A. Badcock, and N. J. Long, "Magnetic AC loss characteristic of 2G Roebel cable," *IEEE Trans. Appl. Supercond.*, vol. 19, no. 3, pp. 3361–3364, Jun. 2009.

[16] L. Lakshmi, M. P. Staines, K. Thakur, R. A. Badrock, and N. J. Long, "Frequency dependence of magnetic AC loss in a five strand YBCO Roebel cable," *Supercond. Sci. Technol.*, vol. 23, no. 6, Apr. 2010, Art. ID 065008.

[17] L. Lakshmi *et al.*, "Magnetic and transport AC loss in HTS Roebel cable," *IEEE Trans. Appl. Supercond.*, vol. 21, no. 3, pp. 3311–3315, Jun. 2011.

[18] L. Lakshmi *et al.*, "Frequency dependence of magnetic AC loss in a Roebel cable made of YBCO on Ni-W substrate," *Supercond. Sci. Technol.*, vol. 23, no. 8, Jul. 2010, Art. ID 085009.

[19] M. Majoros, M. D. Sumption, E. W. Collings, and N. J. Long, "Stability, inter-strand contact resistance and AC loss in Roebel cables," *IEEE Trans. Appl. Supercond.*, vol. 24, no. 3, Jun. 2014, Art. ID 6600505.

[20] E. Pardo and F. Grilli, "Numerical simulation of the angular dependence of magnetization AC loss: Coated conductors, Roebel cables and double pancake coils," *Supercond. Sci. Technol.*, vol. 25, no. 1, Dec. 2012, Art. ID 014008.

[21] S. Terzieva *et al.*, "Investigation of the effect of striated strands on the AC losses of 2G Roebel cables," *Supercond. Sci. Technol.*, vol. 24, no. 4, Jan. 2011, Art. ID 045001.

[22] P. Horowitz and W. Hill, *The Art of Electronics*, 2nd ed. Cambridge, U.K.: Cambridge Univ. Press, 1989.

[23] A. Ruehli, "Equivalent circuit models for three-dimensional multiconductor systems," *IEEE Trans. Microw. Theory Techn.*, vol. MTT-22, no. 3, pp. 216–221, Mar. 1974.

[24] S. Russenschuck, *Field Computation for Accelerator Magnets*. Hoboken, NJ, USA: Wiley, 2010.

[25] P. Deuflhard, *Newton Methods for Nonlinear Problems, Affine Invariance and Adaptive Algorithms*, ser. Springer Series in Computational Mathematics, vol. 35. Berlin, Germany: Springer-Verlag, 2004.

[26] L. Greengard and V. Rokhlin, "A fast algorithm for particle simulations," *J. Comput. Phys.*, vol. 135, no. 2, pp. 325–348, Aug. 1987.

[27] J. Fleiter and A. Ballarino, "Parameterization of the critical surface of REBCO conductors from Fujikura," CERN, Geneva, Switzerland, Tech. Rep., Oct. 2014.

[28] Y-based High Temperature Superconductor, Fujikura, Tokyo, Japan, 2014.

[29] J. Ekin, *Experimental Techniques for Low-Temperature Measurements*. London, U.K.: Oxford Univ. Press, 2006.

[30] K. Yagotintsev *et al.*, "AC loss tests on CORC and stacked tape ReBCO cables," presented at the Applied Superconductivity Conf., Charlotte, NC, USA, Aug. 2014.

[31] B. Wadell, *Transmission Line Design Handbook*. Norwood, MA, USA: Artech House, 1991.

[32] F. Grouvers, *Inductance Calculations*. New York, NY, USA: Van Nostrand, 1946.

[33] F. Grover, *Inductance Calculations*. New York, NY, USA: Dover, 2004.

[34] E. P. A. Van Lanen and A. Nijhuis, "Simulation of interstrand coupling loss in cable-in-conduit conductors with JackPot-AC," *IEEE Trans. Appl. Supercond.*, vol. 21, no. 3, pp. 1926–1929, Jun. 2011.

[35] E. van Lanen, J. van Nugteren, and A. Nijhuis, "Full-scale calculation of the coupling losses in ITER size cable-in-conduit conductors," *Supercond. Sci. Technol.*, vol. 25, no. 2, Dec. 2012, Art. ID 025012.

[36] A. Hindmarsh *et al.*, "SUNDIALS: Suite of nonlinear and differential/algebraic equation solvers," *ACM Trans. Math. Softw.*, vol. 31, no. 3, pp. 363–396, Sep. 2005.

[37] A. Hindmarsh *et al.*, "SUNDIALS: Suite of nonlinear and differential/algebraic equation solvers," Lawrence Livermore Nat. Lab., Livermore, CA, USA, LLNL Tech. Rep. UCRL-JP-200037.

[38] CTD-101G, Cryogenic, Alumina Filled, Anhydride Cured Epoxy, Composite Technology Development, Lafayette, CO, USA, 2006. [Online]. Available: http://www.CTD-materials.com

[39] Fuji Pressure Sensitive Film, Feltest. [Online]. Available: http://www.feltest.com

[40] F. Grilli, E. Pardo, and A. Stenvall, "Computation of losses in HTS under the action of varying magnetic fields and currents," *IEEE Trans. Appl. Supercond.*, vol. 24, no. 1, Feb. 2014, Art. ID 8200433.

[41] V. Zermeno, F. Grilli, and F. Sirois, "A full 3-D time-dependent electromagnetic model for Roebel cables," *Supercond. Sci. Technol.*, vol. 26, no. 5, May 2013, Art. ID 052001.